GEOPHYSICS, VOL. 84, NO. 6 (NOVEMBER-DECEMBER 2019); P. B353–B361, 15 FIGS., 1 TABLE.
10.1190/GEO2018-0848.1

Check for updates

Downloaded 10/14/19 to 136.252.129.67. Redistribution subject to SEG license or copyright; see Terms of Use at http://library.seg.org/

Case History

Rock physics of the Wolfcamp Formation, Delaware Basin

Colin M. Sayers[1], Sagnik Dasgupta[2], Adam Koesoemadinata[1], and Michael Shoemaker[3]

ABSTRACT

Production from wells in organic-rich shales often shows considerable lateral variation. Reliable predrill methods to characterize the lateral heterogeneity of such reservoirs are required to optimize the trajectory of lateral wells in these low-permeability reservoirs. Petrophysical interpretation of measured well logs provides information on mineral, porosity, and kerogen content. Combining the results of petrophysical analysis with P-wave, S-wave, and density logs allows generation of a probability density function (PDF) for each of the different significant lithofacies. The PDFs are applied to the P- and S-impedance from prestack seismic amplitude variation with offset inversion to predict the spatial variation in the distribution of lithofacies and associated probability for the Wolfcamp Formation in an area covered by a 3D seismic survey in the Delaware Basin, West Texas. An anisotropic rock-physics model for the Wolfcamp Formation allows the effect of complex mineralogy, organic carbon concentration, and porosity on the P- and S-impedance to be investigated. Kerogen inclusions and pores act to increase Thomsen's anisotropy parameter ε relative to γ, and there is a competition between clay matrix anisotropy and inclusion shape anisotropy in determining the anisotropy of the rock. Inclusions with isotropic elastic properties act to decrease the anisotropy due to the dilution effect, but this decrease is partially offset by the increase in anisotropy due to the anisotropic shape of the inclusions. Application of the model to the determination of minimum horizontal stress indicates that kerogen-rich siliceous shales have the lowest value of minimum horizontal stress, whereas silica-rich calcareous shales, mixed siliceous shales, and clay-rich siliceous shales have higher values and may therefore act as barriers for the vertical growth of hydraulic fractures.

INTRODUCTION

Shales make up a large proportion of the rocks in most sedimentary basins and form the seal and source rocks for many hydrocarbon reservoirs. Organic-rich shales represent an enormous energy resource, but production from wells in such plays may show considerable lateral variation. An example is the Wolfcamp Formation of the Delaware Basin, West Texas. The Delaware Basin is the western subbasin of the Permian Basin. The Wolfcamp Formation is currently being targeted using horizontal drilling. This formation lies over the Pennsylvanian Cisco Formation, and it is overlain by the Leonardian Bone Spring Formation (Hills, 1984; Fairhurst and Hanson, 2013; Yates et al., 2013).

Despite having high potential, the Wolfcamp Formation in the Permian Basin displays heterogeneous petrophysical and geomechanical rock properties, and production logs show that not all fracture stages contribute significantly to production (Yates et al., 2013; Ajisafe et al., 2014; Azike et al., 2014; Sharma et al., 2014), resulting in lateral variations in production. Economic production from tight shale formations requires good reservoir quality (RQ), representing the multiple properties defining the hydrocarbon content and producibility, and good completion quality (CQ), representing the multiple properties defining the potential for creating and sustaining a large surface area in contact with the reservoir (Suarez-Rivera et al., 2011). Reliable predrill methods to determine the spatial variation in RQ and CQ are therefore required

Manuscript received by the Editor 17 December 2018; revised manuscript received 17 June 2019; published ahead of production 25 July 2019; published online 09 October 2019.
[1]Schlumberger, Houston, Texas, USA. E-mail: csayers@slb.com; koesoemadinata@slb.com.
[2]Schlumberger, Calgary, Alberta, Canada. E-mail: sdasgupta@slb.com.
[3]Callon Petroleum, Houston, Texas, USA. E-mail: mshoemaker@callon.com.
© 2019 Society of Exploration Geophysicists. All rights reserved.

Downloaded 10/14/19 to 136.252.129.67. Redistribution subject to SEG license or copyright; see Terms of Use at http://library.seg.org/

to optimally locate wells in low-permeability reservoirs such as the Wolfcamp Formation.

Amplitude variation with offset (AVO) of seismic waves reflected from an interface between two geologic layers can be used to determine the vertical P-impedance, $I_P = \rho V_P$, and vertical S-impedance, $I_S = \rho V_S$, where V_P, V_S, and ρ are the vertical P-wave velocity, vertical S-wave velocity, and density of the rock, respectively. To obtain predrill information on RQ and CQ, a rock-physics model is required that relates the inverted P- and S-impedance to properties of the rock such as the volume fractions of quartz, carbonates, clays, kerogen, and geomechanical properties. Herein, we present an anisotropic rock-physics model for the Wolfcamp Formation in the Delaware Basin.

LOG DATA

The log data used herein are from a vertical well in the Wolfcamp Formation of the Delaware Basin in which various types of open-hole logging data were acquired. In the Delaware Basin, the Wolfcamp Formation is composed primarily of dark shales and interbedded detrital carbonates (Yates et al., 2013; Ajisafe et al., 2014; Azike et al., 2014; Sharma et al., 2014). Figure 1 shows a plot of the variation with depth of lithology, vertical P-impedance, and vertical S-impedance for the well that is considered in this work. The high-impedance carbonates are clearly visible.

Figure 2 shows a plot of vertical S-impedance I_S versus vertical P-impedance I_P for the Wolfcamp interval in this well, with points color coded by volume fraction of kerogen. The lines in Figure 2 are lines of constant $V_P/V_S = I_P/I_S$. Increasing the kerogen content is seen to lower the acoustic impedance I_P, shear impedance I_S, and V_P/V_S, consistent with previous work for the Bossier/Haynesville Shale (Lucier et al., 2011) and the Eagle Ford, Woodford, Haynesville, and Bakken Shales (Khadeeva and Vernik, 2013). Vernik and Milovac (2011) suggest that the lower values of V_P/V_S seen in organic-rich shales are due to the presence of the solid organic matter. S-wave information, as can be obtained from AVO inversion may therefore be used to distinguish organic-rich shales from other lithologies that may be present (Hu et al., 2015).

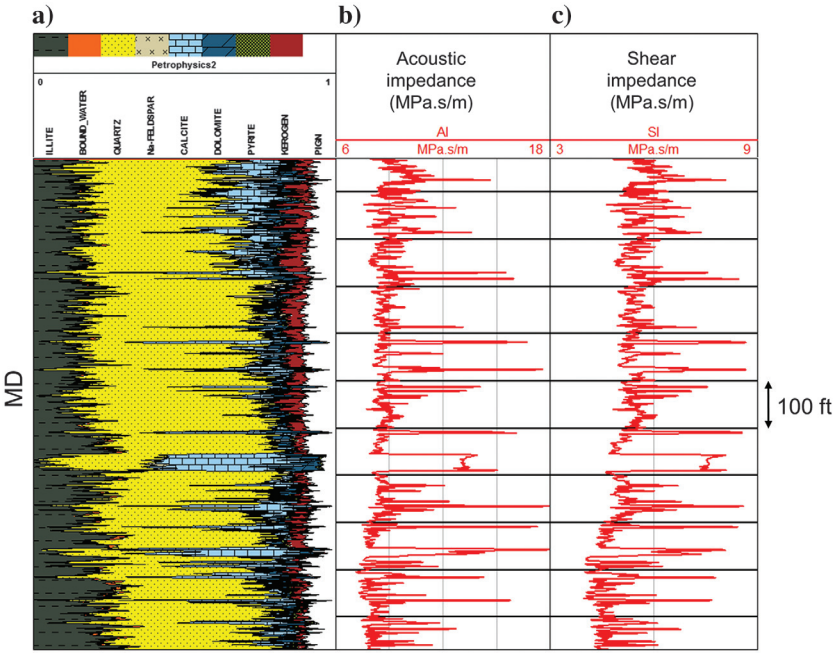

Figure 1. Variation in lithology showing (a) volume fraction of clays (illite and associated bound water), quartz, Na-feldspar, carbonate (calcite and dolomite), pyrite, and effective porosity, (b) vertical P-impedance, and (c) vertical S-impedance for the Wolfcamp Formation sampled by the vertical well.

PETROPHYSICS AND ROCK CLASSIFICATION

The petrophysical analysis is based on elemental spectroscopy, nuclear magnetic resonance (NMR), neutron, density, and resistivity logs. Mineralogy and kerogen are estimated from inelastic and capture spectroscopy measurements, whereas porosity and fluid saturation are estimated by combining NMR, neutron, density, and resistivity measurements. The rock is made of three major mineral groups: clay, silicates, and carbonates. Clay minerals consist mostly of illite, silicates consist mainly of quartz and Na-feldspar, and carbonates consist principally of calcite and dolomite. The rock also contains up to 4% pyrite by volume. The effective porosity of the rock ranges from 0% to 15%. Kerogen varies from 0% to 14% by volume. In the Wolfcamp Formation, several mineralogical cycles are observed and are marked by stratigraphic markers. The stratigraphic boundaries are associated with a sharp decrease of carbonate content and an increase of siliciclastic materials within the reservoir section. Higher values of porosity and kerogen content are associated with the presence of siliciclastic minerals. During maturation, kerogen adds porosity, which acts to improve RQ by providing pore volume and flow pathways for the production of hydrocarbon. In addition, kerogen acts to decrease Poisson's ratio (Vernik and Milovac, 2011; Khadeeva and Vernik, 2013) and it therefore acts to increase CQ by reducing the minimum horizontal stress (Thiercelin and Plumb, 1991; Savage et al., 1992) thus allowing fracture opening at a lower pressure in the fracture.

The rock composition is important in characterizing elastic properties, such as the elastic moduli and the P- and S-impedance. Figure 3 shows the mineralogical composition of the inorganic phase for the depth interval shown in Figure 1, color coded by the volume fraction of kerogen. All carbonates (calcite and dolomite), silicates (quartz and feldspar), and clay minerals (mainly illite) are combined and normalized to produce the ternary plot shown in Figure 3.

Volume fractions of carbonate, clay, and quartz-feldspar were used to perform a classification of the reservoir. Principal component analysis was performed with these volumes to reduce the dimension of the data and to find the orthogonal set of components required to explain the multidimensional space. K-means clustering was used to find the clusters with the principal components. A total of four classes were identified from the volume fractions, as shown in Figure 4. The location of the different lithoclasses on a plot of I_S versus I_P is shown in Figure 5.

Probability density functions (PDFs) or posterior cumulative density functions are computed

Downloaded 10/14/19 to 136.252.129.67. Redistribution subject to SEG license or copyright; see Terms of Use at http://library.seg.org/

by combining the prior distribution of the model properties with the likelihood function of the data given the model properties. In this case, the prior distribution of each class and the associated property distribution are estimated from well-log-derived I_P, V_P/V_S, and petrophysical interpretation. Bayesian methods allow estimation of the most likely solution of the inverse problem and quantification of the associated uncertainty or probability through statistical estimators of the posterior probability distribution, such as the standard deviation or the percentiles.

Figure 6 shows I_P and V_P/V_S obtained from AVO inversion for an inline passing through the vertical well with logs shown in Figure 1. Also shown is the resulting lithoclassification based on the maximum a posteriori estimate provided by the Bayesian analysis. The P-impedance and V_P/V_S shown in Figure 6 were obtained using isotropic AVO inversion. If anisotropy is present, this implies that the inverted value of V_P/V_S will be shifted from the true value as may be seen from the work of Plessix and Bork (2000), who show that instead of the shear impedance I_S, isotropic AVO inversion will give the combined parameter $I_S(1-\delta/2)$, where δ is Thomsen's anisotropy parameter. However, the P-impedance and V_P/V_S shown in Figure 6 are seen to be in good agreement with the log values, so no correction is necessary. This occurs because the inversion uses a separate wavelet for each angle stack, obtained by calibrating to the upscaled log P-impedance and V_P/V_S, which compensates for the effects of δ, NMO stretch, frequency variation with offset, and energy variation with offset. Figure 7 shows the probability of the various classes that result.

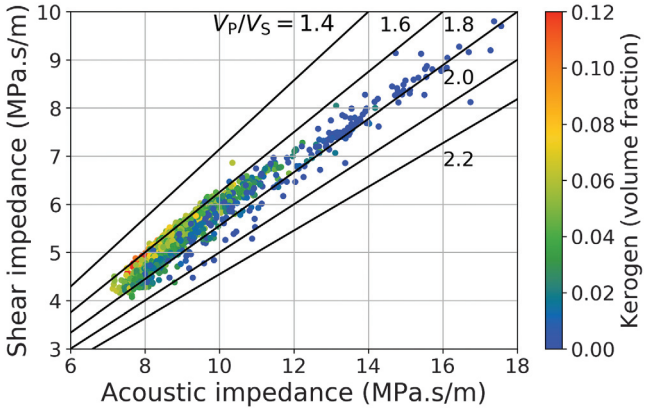

Figure 2. Plot of vertical S-impedance I_S versus vertical P-impedance I_P for the Wolfcamp shale sampled by the vertical well, with points color coded by the volume fraction of kerogen. The lines correspond to constant $I_P/I_S(=V_P/V_S) = 1.4$ (top), 1.6, 1.8, 2.0, and 2.2 (bottom).

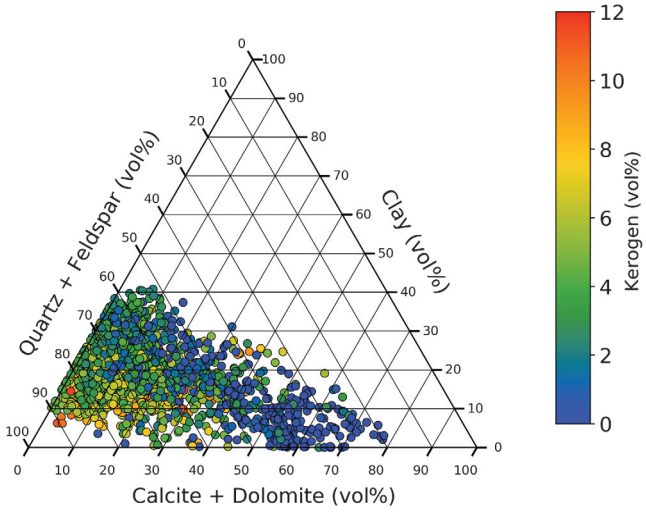

Figure 3. Mineralogical composition of the inorganic phase for the depth interval shown in Figure 1, color coded by the volume percentage of kerogen.

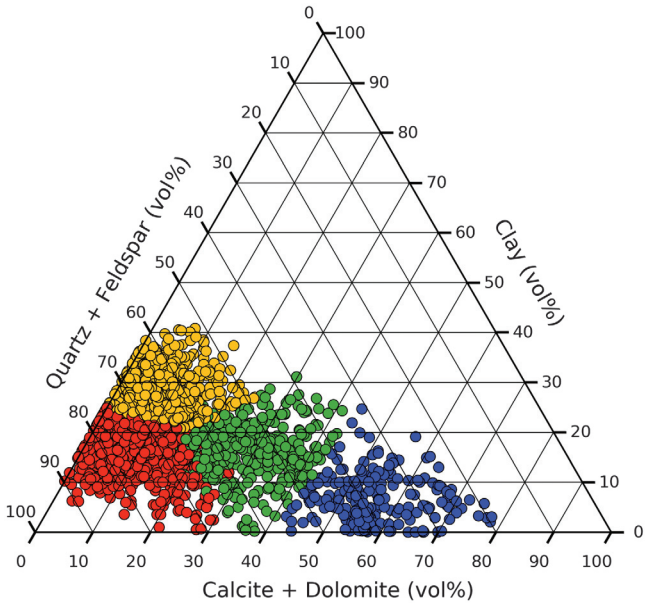

Figure 4. Mineralogical composition of the inorganic phase for the depth interval shown in Figure 1, color coded by lithoclass as follows: kerogen-rich siliceous shales (the red points), silica-rich calcareous shales (the blue points), mixed siliceous shales (the green points), and clay-rich siliceous shales (the yellow points).

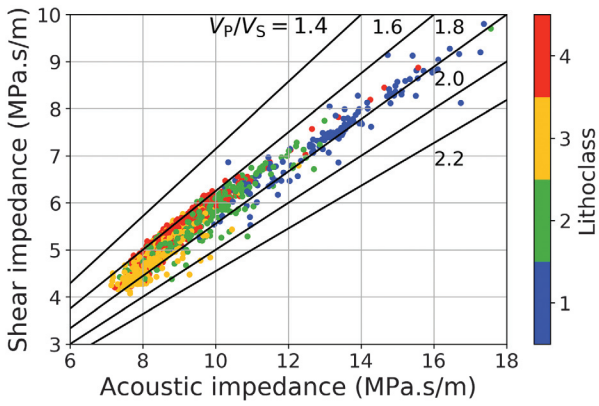

Figure 5. Plot of vertical S-impedance I_S versus vertical P-impedance I_P color coded by lithoclass as follows: kerogen-rich siliceous shales (the red points), silica-rich calcareous shales (the blue points), mixed siliceous shales (the green points), and clay-rich siliceous shales (the yellow points). The lines correspond to constant $I_P/I_S(=V_P/V_S) = 1.4$ (top), 1.6, 1.8, 2.0, and 2.2 (bottom).

Downloaded 10/14/19 to 136.252.129.67. Redistribution subject to SEG license or copyright; see Terms of Use at http://library.seg.org/

ROCK-PHYSICS MODEL

The Wolfcamp Formation shown in Figure 1 is highly laminated with alternate layers of silicate- and carbonate-rich units. Although the carbonate-rich units are lower in porosity, the silicate-rich units contain a significant volume concentration of kerogen and effective porosity ϕ_{eff} with values up to 0.14 and 0.15, respectively.

Due to fine layering and the presence of organic material, with partial alignment with the bedding plane, organic-rich shales often display elastic anisotropy, and this can be described, to a good approximation, by transverse isotropy (TI) with the axis of rotational symmetry oriented perpendicular to the bedding. A TI medium has five independent elastic stiffnesses. Taking the x_3-axis to lie along the axis of rotational symmetry, the nonvanishing elastic stiffness coefficients are $C_{11} = C_{22}$, C_{33}, $C_{44} = C_{55}$, C_{66}, $C_{12} = C_{11} - 2C_{66}$, and $C_{13} = C_{23}$ in the conventional two-index notation (Nye, 1985). The elastic anisotropy of a transversely isotropic medium can be described by the three anisotropy parameters ε, γ, and δ defined by Thomsen (1986) as given by the following equations:

$$\varepsilon = \frac{C_{11} - C_{33}}{2C_{33}}, \quad \gamma = \frac{C_{66} - C_{55}}{2C_{55}}, \quad \delta = \frac{(C_{13} + C_{55})^2 - (C_{33} - C_{55})^2}{2C_{33}(C_{33} - C_{55})}. \tag{1}$$

Assuming that the intrinsic anisotropy of the formation is zero, with bulk and shear moduli calculated from compressional, shear, and density logs, Backus upscaling (Backus, 1962) with averaging window covering the entire depth range shown in Figure 1, gave the values $\varepsilon = 0.032$, $\gamma = 0.041$, and $\delta = -0.007$. These values are significantly lower than the typical anisotropy of organic-rich shales (e.g., Bocangel et al., 2013; Vernik, 2016), and this shows that upscaling of isotropic layers cannot account for the measured anisotropy of the Wolfcamp, which appears to be primarily due to the intrinsic anisotropy of the shale.

To investigate the sensitivity of I_P, I_S, and anisotropy to variations in mineralogy, effective porosity, and kerogen content, Maxwell's homogenization scheme (Maxwell, 1873) extended to the determination of the anisotropic elastic properties of a transversely isotropic medium containing inhomogeneities by Sevostianov and Giraud (2013), Sevostianov (2014), and Vilchevskaya and Sevostianov (2015) was used. This approach is formulated in terms of the fourth-rank compliance contribution tensor $\mathbf{H}_r$ that gives the extra strain per reference volume V when an inhomogeneity with volume V_r and compliance tensor $\mathbf{S}^{(r)}$ is placed in a homogeneous elastic matrix with compliance tensor $\mathbf{S}^{(0)}$ and stiffness tensor $\mathbf{C}^{(0)} = \mathbf{S}^{(0)^{-1}}$. Extending Maxwell's scheme to anisotropy, Sevostianov and coworkers (Sevostianov and Giraud, 2013; Sevostianov, 2014; Sevostianov and Kachanov, 2014; Vilchevskaya and Sevostianov, 2015) consider the far-field strain produced by a domain Ω of volume V^* cut from a heterogeneous medium and placed in the matrix material. They obtain the following expression for the compliance tensor of the heterogeneous medium:

$$\mathbf{S}^{\text{eff}} = \mathbf{S}^{(0)} + \left[\left(\frac{1}{V^*}\sum_r V_r \mathbf{H}_r\right)^{-1} - \mathbf{Q}_\Omega\right]^{-1}. \tag{2}$$

Here

$$\mathbf{Q}_\Omega = \mathbf{C}^{(0)} : (\mathbf{I} - \mathbf{P}_\Omega : \mathbf{C}^{(0)}). \tag{3}$$

The components P_{ijkl} of the fourth-rank tensor $\mathbf{P}_\Omega$ are obtained from the equation:

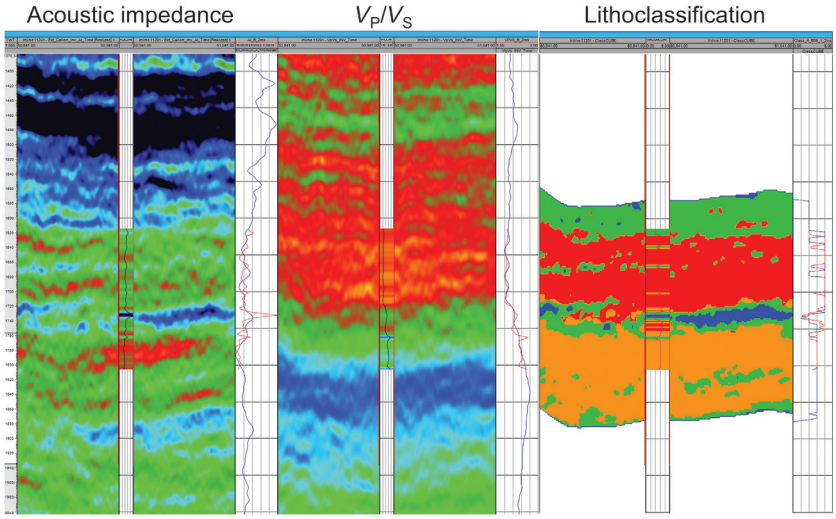

Figure 6. Plot of I_P and V_P/V_S (red, low; blue, high) obtained from AVO inversion for an inline passing through the vertical well with logs shown in Figure 1. Also shown is the resulting lithoclassification, with color coding the same as in Figure 4. Figure 7 shows the probability of the various classes.

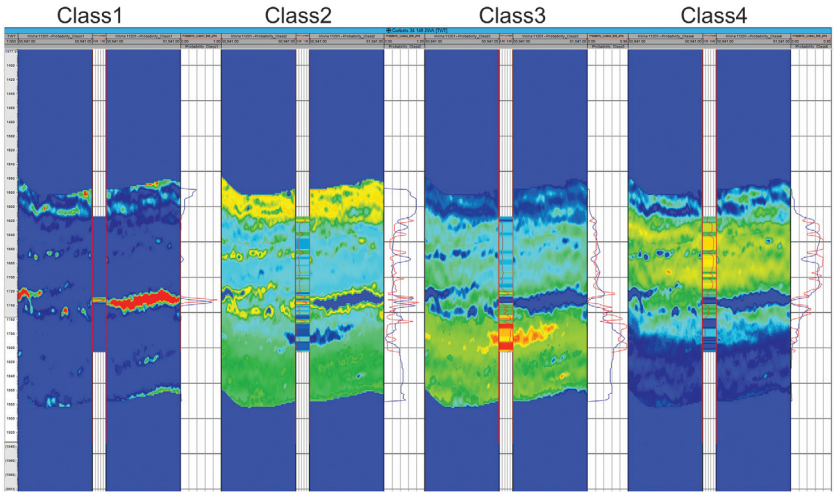

Figure 7. Probability (red, high; blue, low) of class 1 (silica-rich calcareous shale), class 2 (mixed siliceous shale), class 3 (clay-rich siliceous shale), and class 4 (kerogen-rich siliceous shale).

$$P_{ijkl} = \int_{\Omega} G_{ik,lj}(x - x')dx'|_{(ij)(kl)}, \quad (4)$$

by integrating over the domain Ω of the effective inclusion. The term $G(x)$ is the elastic Green's function of the anisotropic infinite medium. The comma followed by subscripts l and j denotes the spatial derivatives with respect to the coordinates x_l and x_j and the symbol (ij) denotes the symmetrization over the included indices ij. We assume that the shape of the effective inclusion is spherical, as in Maxwell's original work. The effective elastic stiffness tensor $\mathbf{C}^{\text{eff}} = \mathbf{S}^{\text{eff}^{-1}}$ is obtained by inverting the compliance tensor.

Phase (0) in equation 2 is assumed to be clay. The kerogen inclusions and pores were modeled as oblate spheroids, whereas the other components were assumed to be spherical. An oblate spheroid is an ellipsoid obtained by rotating an ellipse about its minor axis, with the equatorial dimension a greater than the polar dimension c. The minor axes of the kerogen inclusions and pores are assumed to be aligned parallel to x_3, with aspect ratio $c/a = 0.2$.

Several published values of the elastic properties of clay were tried; the best agreement with the P- and S-impedance calculated from the available well logs being obtained using the elastic stiffnesses $C_{33} = 24.2$ and $C_{55} = 3.7$ GPa obtained by Ulm and Abousleiman (2006) and Ortega et al. (2007) using nano- and microindentation. However, the results obtained using the Thomsen anisotropy parameters $\varepsilon = 0.4277$, $\delta = 0.0554$, and $\gamma = 1.0676$ calculated from the elastic stiffnesses given by Ulm and Abousleiman (2006) and Ortega et al. (2007) did not give good agreement with the anisotropy parameters ε and γ measured on core, and the values $\varepsilon = 0.1$, $\delta = 0.05$, and $\gamma = 0.15$ gave better agreement with the data. Figure 8 shows the plot of I_S versus I_P that results. Table 1 lists the values of K and μ for the other minerals and kerogen used in the modeling. The values for quartz, feldspar, calcite, dolomite, and pyrite were taken from the table in section 10.3 of work by Mavko et al. (2009). The values for kerogen were taken from Vernik (2016). Overall, the predictions are in reasonable agreement with the measured values shown in Figure 2, as may also be seen in Figures 9 and 10,

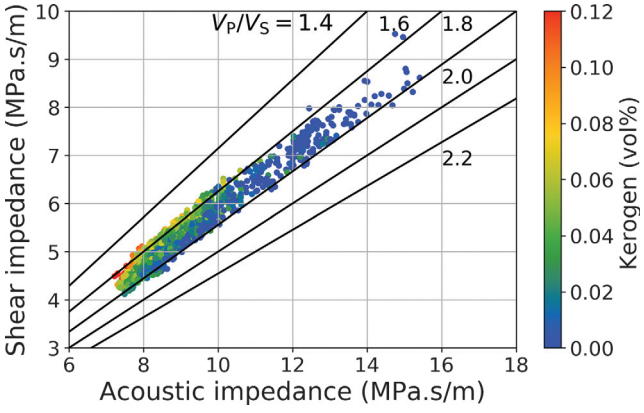

Figure 8. Plot of vertical S-impedance I_S versus vertical P-impedance I_P calculated for the Wolfcamp interval using Maxwell's homogenization scheme, extended to the determination of the anisotropic elastic properties of a transversely isotropic medium containing inhomogeneities by Sevostianov and Giraud (2013), Sevostianov (2014), and Vilchevskaya and Sevostianov (2015). The lines correspond to constant $I_P/I_S(= V_P/V_S) = 1.4$ (top), 1.6, 1.8, 2.0, and 2.2 (bottom).

Table 1. Elastic properties assumed for the different rock constituents included in the rock-physics model.

Minerals	K (GPa)	μ (GPa)	References
Quartz	37.9	44.3	McSkimin et al. (1965)
Feldspar	37.5	15	Mavko et al. (2009)
Calcite	76.8	32.0	Simmons (1965)
Dolomite	94.9	45.0	Humbert and Plicque (1972)
Pyrite	138.6	109.8	Woeber et al. (1963)
Kerogen	3.9	4.2	Vernik (2016)

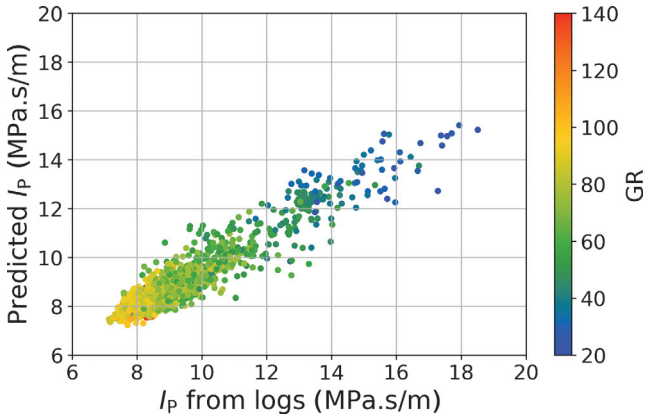

Figure 9. Plot of I_P calculated from log data versus I_P calculated for the Wolfcamp interval using Maxwell's homogenization scheme, extended to the determination of the anisotropic elastic properties of a transversely isotropic medium containing inhomogeneities by Sevostianov and Giraud (2013), Sevostianov (2014), and Vilchevskaya and Sevostianov (2015).

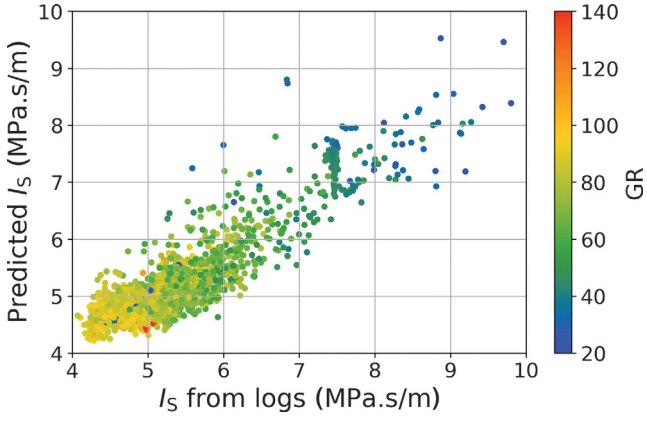

Figure 10. Plot of I_S calculated from log data versus I_S calculated for the Wolfcamp interval using Maxwell's homogenization scheme, extended to the determination of the anisotropic elastic properties of a transversely isotropic medium containing inhomogeneities by Sevostianov and Giraud (2013), Sevostianov (2014), and Vilchevskaya and Sevostianov (2015).

Downloaded 10/14/19 to 136.252.129.67. Redistribution subject to SEG license or copyright; see Terms of Use at http://library.seg.org/

Downloaded 10/14/19 to 136.252.129.67. Redistribution subject to SEG license or copyright; see Terms of Use at http://library.seg.org/

which compare the P- and S-impedances computed from the logs with the values predicted using the rock-physics model described above.

Figures 11 and 12 show plots of ε versus γ and δ versus ε calculated for the Wolfcamp interval shown in Figure 1, color coded by the volume fraction of kerogen. The variation of ε with γ is seen to be consistent with the core data shown by the red points. It is seen that ε is predicted to be greater than γ despite the fact that a value of ε less than the value of γ was assumed for clay. This shows that the kerogen inclusions and pores act to increase ε relative to γ. Figure 12 shows that δ is increased over the value assumed for clay, but for a given value of ε, δ decreases with the increasing volume fraction of kerogen. It should be noted that there is a competition between clay matrix anisotropy and anisotropy resulting from the partial alignment of low-aspect-ratio kerogen inclusions and pores in determining the anisotropy of the medium. The elastic properties of the kerogen inclusions and pores are assumed to be isotropic. This would lead to a decrease in anisotropy due to the dilution effect, but this decrease is partially offset by the increase in anisotropy due to the anisotropic shape of the inclusions.

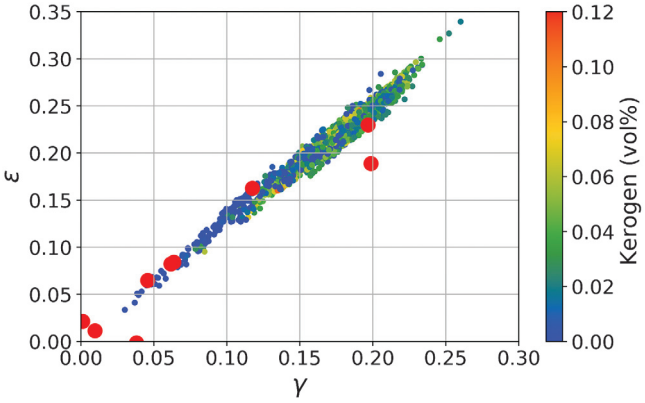

Figure 11. Plot of ε versus γ calculated for the Wolfcamp interval, color coded by volume fraction of kerogen, compared with core measurements (the red points).

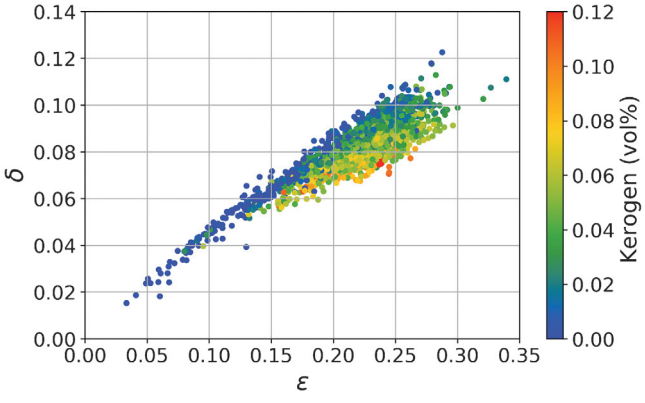

Figure 12. Plot of δ versus ε calculated for the Wolfcamp interval, color coded by volume fraction of kerogen.

DISCUSSION

The rock-physics model presented in this paper can account for the variable mineralogy present in unconventional reservoirs. This allows prediction of the elastic properties given information on the composition of the rock, as may be obtained using elemental capture spectroscopy, for example. To do so requires knowledge of the elastic properties of the various rock constituents. Although the elastic properties of minerals such as quartz, feldspar, calcite, dolomite, and pyrite are widely available (e.g., Mavko et al., 2009), the elastic properties of kerogen and clay are less well-known. In this paper, the properties of kerogen were taken from Vernik (2016). Although several published values of the elastic properties of clay were tried, the best agreement with the P- and S-impedance calculated from the available well logs was obtained using the elastic stiffnesses $C_{33} = 24.2$ and $C_{55} = 3.7$ GPa obtained by Ulm and Abousleiman (2006) and Ortega et al. (2007) using nano- and microindentation. However, the results obtained using the Thomsen anisotropy parameters $\varepsilon = 0.4277$, $\delta = 0.0554$, and $\gamma = 1.0676$ calculated from the elastic stiffnesses given by Ulm and Abousleiman (2006) and Ortega et al. (2007) did not give good agreement with the anisotropy parameters ε and γ measured on the core and plotted in Figure 11, and the values $\varepsilon = 0.1$, $\delta = 0.05$, and $\gamma = 0.15$ gave a better agreement with the data.

Because of the variability of the elastic properties of clay and the dependence of the bulk and shear moduli of kerogen on maturity, the model needs to be calibrated using compressional, shear, and density logs together with volume fractions of the various rock constituents obtained by petrophysical analysis. Although suitable log data may be available in vertical pilot holes allowing calibration of the model for such wells, such data are often not available for lateral wells. For lateral wells, Prioul et al. (2018) develop a method for determining rock composition using diffuse reflectance infrared Fourier transform spectroscopy on drill cuttings. This enables the use of the rock-physics model to predict elastic properties needed for geomechanical calculations in lateral wells based on such measurements.

An important application of the model is in the prediction of minimum horizontal stress because this determines the pressure required to open a hydraulic fracture. Assuming TI with a vertical axis of rotational symmetry, and that one of the principal axes of the stress tensor is vertical, the minimum horizontal stress σ_h may be estimated using the following equation derived by Thiercelin and Plumb (1991) and Savage et al. (1992) using anisotropic poroelasticity:

$$\sigma_h = \alpha_h p + K_0(\sigma_V - \alpha_V p) + \frac{E}{(1-\nu^2)}(\varepsilon_h + \nu\varepsilon_H), \quad (5)$$

where σ_V is the vertical stress, p is the pore pressure, α_h and α_V are the poroelastic coefficients, E is the horizontal Young's modulus, ν is the Poisson's ratio that relates the expansion that occurs in a horizontal direction to a compression applied along a perpendicular horizontal direction, and ε_h and ε_H are the elastic strains in the minimum σ_h and maximum σ_H directions, respectively. For a VTI medium (a TI medium with a vertical axis of rotational symmetry), the coefficient K_0 of the second term on the right side of equation 5 is given by

$$K_0^{\mathrm{VTI}} = C_{13}/C_{33}, \tag{6}$$

where x_3 is chosen as the axis of rotational symmetry.

Figure 13 plots the coefficient $K_0^{\mathrm{VTI}} = C_{13}/C_{33}$ computed by the rock-physics model as a function of the gamma ray (GR). This shows that if the horizontal elastic strains ε_h and ε_H are ignored, kerogen-rich siliceous shales (the red points) have the lowest value of minimum horizontal stress according to equation 5, whereas silica-rich calcareous shales (the blue points), mixed siliceous shales (the green points), and clay-rich siliceous shales (the yellow points) have higher values of C_{13}/C_{33} and may therefore act as barriers for the vertical growth of hydraulic fractures due to the higher values of minimum horizontal stress predicted in equation 5. This information can be populated for the whole survey using the probability cubes from each facies. Mapping of C_{13}/C_{33} in this way is expected to help optimize hydraulic fracturing of lateral wells.

For comparison, if the medium is assumed to be isotropic, K_0 is given by

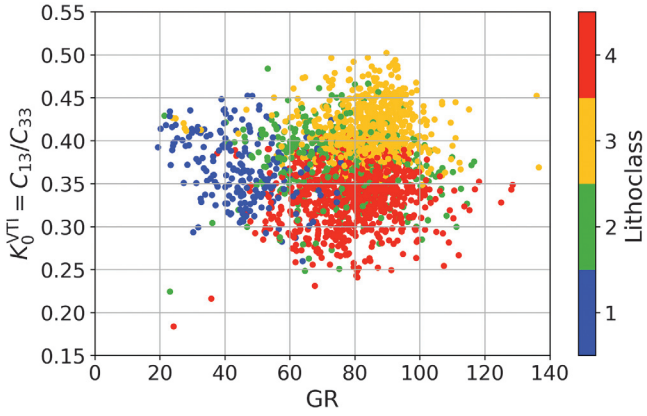

Figure 13. Plot of $K_0^{\mathrm{VTI}} = C_{13}/C_{33}$ as a function of GR. The points are color coded by lithoclass as follows: kerogen-rich siliceous shales (the red points), silica-rich calcareous shales (the blue points), mixed siliceous shales (the green points), and clay-rich siliceous shales (the yellow points).

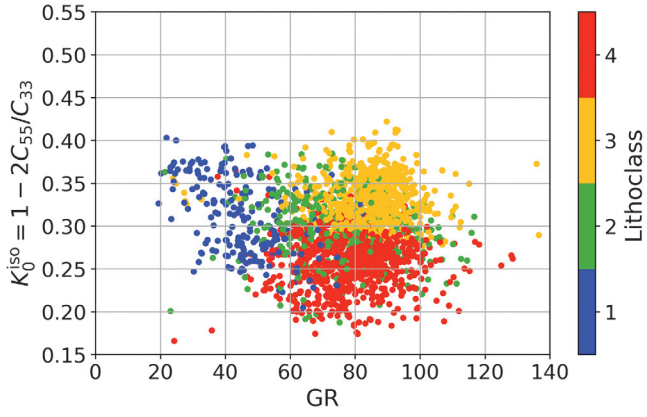

Figure 14. Plot of $K_0^{\mathrm{iso}} = 1 - 2C_{55}/C_{33}$ as a function of GR. The points are color coded by lithoclass as follows: kerogen-rich siliceous shales (the red points), silica-rich calcareous shales (the blue points), mixed siliceous shales (the green points), and clay-rich siliceous shales (the yellow points).

$$K_0^{\mathrm{iso}} = \nu/(1-\nu), \tag{7}$$

where ν is the isotropic Poisson's ratio that can be estimated from the value of $C_{33}/C_{55} = V_P^2/V_S^2$ from seismic inversion as

$$\nu = \frac{(C_{33}/C_{55} - 2)}{2(C_{33}/C_{55} - 1)}. \tag{8}$$

This gives

$$K_0^{\mathrm{iso}} = 1 - \frac{2C_{55}}{C_{33}}. \tag{9}$$

Figure 14 plots $K_0^{\mathrm{iso}} = 1 - 2C_{55}/C_{33}$ computed by the rock-physics model as a function of GR. Figure 15 shows that anisotropy acts to increase K_0 for all facies, in agreement with the conclusions of Shoemaker et al. (2019). The relation between K_0^{VTI} and K_0^{iso} follows from equations 6 and 9 as

$$K_0^{\mathrm{VTI}} = K_0^{\mathrm{iso}} + \chi, \tag{10}$$

where

$$\chi = \frac{(C_{13} + 2C_{55} - C_{33})}{C_{33}}. \tag{11}$$

The term χ is related to Thomsen's δ parameter because (Sayers, 1995)

$$\delta = \chi + \frac{\chi^2}{2(1 - C_{55}/C_{33})}. \tag{12}$$

Because Thomsen's δ parameter is predicted to be positive (see Figure 12), this explains why K_0^{VTI} shown in Figure 13 is higher than K_0^{iso} shown in Figure 14 (see also Vernik and Milovac, 2011). A comparison between K_0^{VTI} and K_0^{iso} is shown in Figure 15.

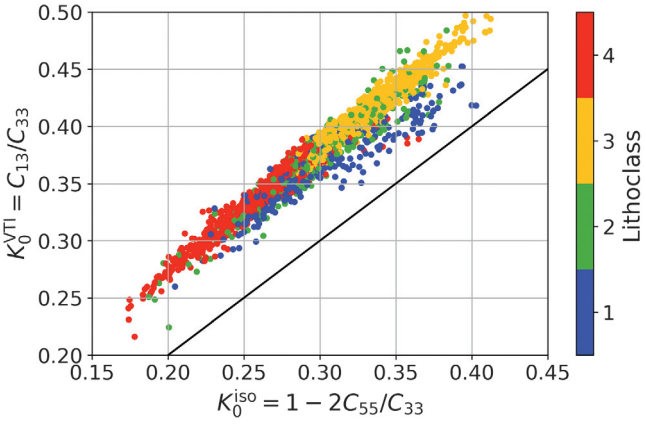

Figure 15. Plot of variation of $K_0^{\mathrm{VTI}} = C_{13}/C_{33}$ with $K_0^{\mathrm{iso}} = 1 - 2C_{55}/C_{33}$. The points are color coded by lithoclass as follows: kerogen-rich siliceous shales (the red points), silica-rich calcareous shales (the blue points), mixed siliceous shales (the green points), and clay-rich siliceous shales (the yellow points). The black line corresponds to $K_0^{\mathrm{VTI}} = K_0^{\mathrm{iso}}$.

Downloaded 10/14/19 to 136.252.129.67. Redistribution subject to SEG license or copyright; see Terms of Use at http://library.seg.org/

Downloaded 10/14/19 to 136.252.129.67. Redistribution subject to SEG license or copyright; see Terms of Use at http://library.seg.org/

CONCLUSION

Using inverted values of the P- and S-impedance obtained by AVO inversion in an area within the Delaware Basin, West Texas, a Bayesian method was used to predict the different dominant lithologies. The prediction matched lithologies obtained by petrophysical analysis at a well location. The probabilities of the dominant lithoclasses show variability across the area of the seismic survey. The main drilling interest is within the kerogen-rich siliceous shale of the Wolfcamp section. The distribution of the kerogen-rich siliceous shale and its associated probability provides important information for the landing and drilling of lateral wells. The kerogen-rich siliceous shale also shows the highest effective porosity. This variability together with the variability of kerogen and porosity can be estimated by integrating the rock-physics model and the seismic inversion result for each facies volume.

An anisotropic rock-physics model for the Wolfcamp Formation allows the effect of complex mineralogy, organic carbon concentration, and porosity on P- and S-impedance to be investigated. Anisotropy is important because it is required for geomechanical applications such as predicting in situ stress, wellbore stability analysis, and the design of hydraulic fractures. Thomsen's parameter ε is predicted to be greater than γ, in agreement with core measurements, despite the fact that a value of ε less than the value of γ was assumed for clay. This shows that the kerogen inclusions and pores act to increase ε relative to γ. There is a competition between clay matrix anisotropy and anisotropy resulting from the partial alignment of low-aspect-ratio kerogen inclusions and pores in determining the anisotropy of the medium. Inclusions with isotropic elastic properties act to decrease the anisotropy due to the dilution effect, but this decrease is partially offset by the increase in anisotropy due to the anisotropic shape of the inclusions.

The rock-physics-based model allows the effect of variations in porosity, pore and kerogen aspect ratio, rock properties, and pore fluid to be investigated. Potential applications include time-lapse feasibility studies, fluid and lithology prediction from AVO inversion, pore pressure prediction, and geomechanical studies. Application to the determination of minimum horizontal stress shows that kerogen-rich siliceous shales have the lowest value of minimum horizontal stress, whereas silica-rich calcareous shales, mixed siliceous shales, and clay-rich siliceous shales are predicted to have higher values and may therefore act as barriers for the vertical growth of hydraulic fractures.

DATA AND MATERIALS AVAILABILITY

Data associated with this research are confidential and cannot be released.

REFERENCES

Ajisafe, F. O., T. L. Pope, O. Azike, R. Reischman, D. Herman, C. G. Burkhardt, A. S. Helmreich, and M. W. Phelps, 2014, Engineered completion workflow increases reservoir contact and production in the Wolfcamp Shale, West Texas: Presented at the SPE Annual Technical Conference and Exhibition, SPE 170718.

Azike, O., F. Ajisafe, T. Pope, C. Burkhardt, A. Helmreich, and M. Phelps, 2014, 3D structural modeling and property characterization for optimized completion design in the Wolfcamp formation, Delaware basin: Presented at the SPE Unconventional Resources Conference, SPE 168990.

Backus, G. E., 1962, Long-wave elastic anisotropy produced by horizontal layering: Journal of Geophysical Research, **67**, 4427–4440, doi: 10.1029/JZ067i011p04427.

Bocangel, W., C. Sondergeld, and C. Rai, 2013, Acoustic mapping and characterization of organic matter in shales: Presented at the SPE Annual Technical Conference and Exhibition, SPE 166331.

Fairhurst, B., and M. L. Hanson, 2013, Wolfbone oil-saturated, super sweet spot, southern Delaware Basin: Integrated approach from exploration to geologic/reservoir modeling and field development: Unconventional Resources Technology Conference, URTeC 1581854.

Hills, J. M., 1984, Sedimentation, tectonism, and hydrocarbon generation in Delaware basin, West Texas and southeastern New Mexico: AAPG Bulletin, **68**, 250–267.

Hu, R., L. Vernik, L. Nayvelt, and A. Dicman, 2015, Seismic inversion for organic richness and fracture gradient in unconventional reservoirs: Eagle Ford Shale, Texas: The Leading Edge, **34**, 80–84, doi: 10.1190/tle34010080.1.

Humbert, P., and F. Plicque, 1972, Propriétés élastiques des carbonates rhombohédriques monocristallins: calcite, magnésite et dolomite: Comptes Rendus de l'Académie des Sciences de Paris, **275**, 391–394.

Khadeeva, Y., and L. Vernik, 2013, Rock-physics model for unconventional shales: The Leading Edge, **33**, 318–322, doi: 10.1190/tle33030318.1.

Lucier, A. M., R. Hofmann, and L. T. Bryndzia, 2011, Evaluation of variable gas saturation on acoustic log data from the Haynesville Shale gas play, NW Louisiana, USA: The Leading Edge, **30**, 300–311, doi: 10.1190/1.3567261.

Mavko, G., T. Mukerji, and J. Dvorkin, 2009, The rock physics handbook: Tools for seismic analysis of porous media: Cambridge University Press.

Maxwell, J. C., 1873, A treatise on electricity and magnetism: Clarendon Press.

McSkimin, H. J., P. Andreatch, Jr., and R. N. L. Thurston, 1965, Elastic moduli of quartz versus hydrostatic pressure at 25 and -195.8C: Journal of Applied Physics, **36**, 1624–1632, doi: 10.1063/1.1703099.

Nye, J. F., 1985, Physical properties of crystals: Oxford University Press.

Ortega, J. A., F.-J. Ulm, and Y. Abousleiman, 2007, The effect of the nanogranular nature of shale on their poroelastic behavior: Acta Geotechnica, **2**, 155–182, doi: 10.1007/s11440-007-0038-8.

Plessix, R. E., and J. Bork, 2000, Quantitative estimate of VTI parameters from AVA responses: Geophysical Prospecting, **48**, 87–108, doi: 10.1046/j.1365-2478.2000.00175.x.

Prioul, R., R. Nolen-Hoeksema, M. Loan, M. Herron, R. Akkurt, M. Frydman, L. Reynolds, M. Sanchez, G. Graf, H. Karg, and J. Caniggia, 2018, Using cuttings to extract geomechanical properties along lateral wells in unconventional reservoirs: Geophysics, **83**, no. 3, MR167–MR185, doi: 10.1190/geo2017-0047.1.

Savage, W. Z., H. S. Swolfs, and B. Amadei, 1992, On the state of stress in the near-surface of the earth's crust: Pure and Applied Geophysics, **138**, 207–228, doi: 10.1007/BF00878896.

Sayers, C. M., 1995, Simplified anisotropy parameters for transversely isotropic sedimentary rocks: Geophysics, **60**, 1933–1935, doi: 10.1190/1.1443925.

Sevostianov, I., 2014, On the shape of effective inclusion in the Maxwell homogenization scheme for anisotropic elastic composites: Mechanics of Materials, **75**, 45–59, doi: 10.1016/j.mechmat.2014.03.003.

Sevostianov, I., and A. Giraud, 2013, Generalization of Maxwell homogenization scheme for elastic material containing inhomogeneities of diverse shape: International Journal of Engineering Science, **64**, 23–36, doi: 10.1016/j.ijengsci.2012.12.004.

Sevostianov, I., and M. Kachanov, 2014, On some controversial issues in effective field approaches to the problem of the overall elastic properties: Mechanics of Materials, **69**, 93–105, doi: 10.1016/j.mechmat.2013.09.010.

Sharma, A., M. E. Yates, T. Pope, K. Fisher, R. Brown, and L. Honeyman, 2014, Horizontal well development in unconventional resource play using an integrated completion and production workflow: Delaware Basin case study: Presented at the SPE/EAGE European Unconventional Resources Conference and Exhibition, SPE 167708.

Shoemaker, M., S. Narasimhan, S. Quimby, and J. Hawkins, 2019, Calculating far-field anisotropic stress from 3D seismic in the Permian Basin: The Leading Edge, **38**, 96–105, doi: 10.1190/tle38020096.1.

Simmons, G., 1965, Single crystal elastic constants and calculated aggregate properties: Southern Methodist University.

Suarez-Rivera, R., C. Deenadayalu, M. Chertov, R. N. Hartanto, P. Gathogo, and R. Kunjir, 2011, Improving horizontal completions on heterogeneous tight shales: Canadian Unconventional Resources Conference, CSUG/SPE-146998.

Thiercelin, M. J., and R. A. Plumb, 1991, A core-based prediction of lithologic stress contrasts in east Texas formations: Presented at the SPE 21847.

Thomsen, L., 1986, Weak elastic anisotropy: Geophysics, **51**, 1954–1966, doi: 10.1190/1.1442051.

Ulm, F.-J., and Y. Abousleiman, 2006, The nanogranular nature of shale: Acta Geotechnica, **1**, 77–88, doi: 10.1007/s11440-006-0009-5.

Vernik, L., 2016, Seismic petrophysics in quantitative interpretation: SEG.

Vernik, L., and J. Milovac, 2011, Rock physics of organic shales: The Leading Edge, **30**, 318–323, doi: 10.1190/1.3567263.
Vilchevskaya, E., and I. Sevostianov, 2015, Effective elastic properties of a particulate composite with transversely-isotropic matrix: International Journal of Engineering Science, **94**, 139–149, doi: 10.1016/j.ijengsci.2015.05.006.
Woeber, A. F., S. Katz, and T. J. Ahrens, 1963, Elasticity of selected rocks and minerals: Geophysics, **28**, 658–663, doi: 10.1190/1.1439242.
Yates, M. E., A. Sharma, T. Itibrout, L. Smith, K. Fisher, R. Brown, L. Honeyman, and B. Bates, 2013, An integrated approach for optimizing vertical Wolfbone wells in the Delaware Basin: Unconventional Resources Technology Conference, URTeC 1580259.

Downloaded 10/14/19 to 136.252.129.67. Redistribution subject to SEG license or copyright; see Terms of Use at http://library.seg.org/